Biomaterials 287 (2022) 121610

Contents lists available at ScienceDirect

Biomaterials

journal homepage: www.elsevier.com/locate/biomaterials

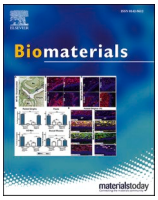

Self-locomotive, antimicrobial microrobot (SLAM) swarm for enhanced biofilm elimination

Yu-Heng Deng [a], Tomas Ricciardulli [a], Jungeun Won [b], Matthew A. Wade [a], Simon A. Rogers [a], Stephen A. Boppart [b,c,d,e], David W. Flaherty [a], Hyunjoon Kong [a,b,d,e,f,g,*]

[a] Department of Chemical and Biomolecular Engineering, University of Illinois at Urbana- Champaign, Urbana, IL, 61801, USA
[b] Department of Bioengineering, University of Illinois at Urbana-Champaign, Urbana, IL, 61801, USA
[c] Department of Electrical and Computer Engineering, University of Illinois at Urbana-Champaign, Urbana, IL, 61801, USA
[d] Beckman Institute, University of Illinois at Urbana-Champaign, Urbana, IL, 61801, USA
[e] Carle Illinois College of Medicine, University of Illinois at Urbana-Champaign, Urbana, IL, 61801, USA
[f] Carl R. Woese Institute for Genomic Biology, University of Illinois at Urbana-Champaign, Urbana, IL, 61801, USA
[g] KU-KIST Graduate School of Converging Science and Technology, Korea University, Seongbuk-gu, Seoul, 02841, South Korea

ARTICLE INFO

Keywords:
Diatom
Polydopamine
MnO_2
Bubble
Wound

ABSTRACT

Biofilm is a major cause of infections and infrastructure deterioration, largely due to molecular diffusion restrictions that hamper the antimicrobial activity of traditional antibiotics and disinfectants. Here, we present a self-locomotive, antimicrobial microrobot (SLAM) swarm that can penetrate, fracture, and detach biofilm and, in turn, nullify bacterial resistance to antibiotics. The SLAM is assembled by loading a controlled mass of manganese oxide nanosheets on diatoms with the polydopamine binder. In hydrogen peroxide solution, SLAMs produce oxygen bubbles that generate thrust to penetrate the rigid and dense *Pseudomonas aeruginosa* biofilm and self-assemble into a swarm that repeatedly surrounds, expands, and bursts oxygen bubbles. The resulting cavities continue to deform and fracture extracellular polymeric substances from microgrooved silicone substrates and wounded skin explants while decreasing the number of viable bacterial cells. Additionally, SLAM allows irrigating water or antibiotics to access the residual biofilm better, thus enhancing the synergistic efficacy in killing up to 99.9% of bacterial cells.

1. Introduction

According to the World Health Organization, a post-antibiotic era is approaching faster than expected due to the increased antimicrobial resistance of microorganisms [1]. In general, bacterial and fungal cells are responsible for various infection cases, such as chronic wound and urinary tract infections [2–5]. These microbial cells also result in infrastructure decay and corrosion, indirectly threatening human health and sustainability [6–9]. Various disinfectants and antibiotics are available to inhibit cell growth or kill cells, but their efficacy in treating microbial cells in biofilms is extremely low because of limited diffusion within extracellular polymer substances (EPS) [10–12]. Therefore, microbial cells in biofilms may be 10–1000 times more resistant to antibiotics than free-floating, planktonic cells [13–15] As a result, antibiotics administered to biofilm kill microbial cells only at the biofilm margin while allowing those deep inside the biofilm to remain viable [10,16].

As such, biofilm removal strategies increasingly center on administering antimicrobial agents within biofilms to enhance drug efficacy [17–22]. In most scenarios, antimicrobials are loaded into nanocarriers like liposomes [20] and polymeric nanoparticles [22] for delivery. Those nanocarriers not only can protect antimicrobials from deactivating substances in biofilms (e.g. antibiotic-inactivating enzymes) [17,20,23] but also can penetrate biofilms through the interaction between nanocarriers and EPS matrix or bacterial cells (e.g. electrostatic interaction) [21,24]. Furthermore, on-demand or selective delivery of antimicrobial agents into biofilms can be achieved by modifying the structures of nanocarriers with stimuli-responsive molecules that target endogenous enzymes and lower pH in the biofilm environment [25–27]. However, even though nanocarriers improve antimicrobial efficacy to kill bacteria, a significant fraction of the EPS remains to rebuild new biofilms. Thus, it is imperative to develop new strategies to combat

* Corresponding author. Department of Chemical and Biomolecular Engineering, University of Illinois at Urbana- Champaign, Urbana, IL, 61801, USA.
E-mail address: hjkong06@illinois.edu (H. Kong).

https://doi.org/10.1016/j.biomaterials.2022.121610
Received 1 May 2022; Accepted 29 May 2022
Available online 3 June 2022

biofilm by simultaneously removing EPS and killing bacterial cells.

Recently, we demonstrated that diatoms engineered to generate oxygen bubbles could invade and fracture *Escherichia coli* biofilm in confined space [28]. To the best of our knowledge, this is the first active matter design for biofilm removal application. Then, similar micro/-nanorobots have been reported to clean biofilms mainly formed on an open and flat surface [29–37]. However, mechanical rigidity and density of biofilm vary with microbial cell types and host structure [38]. For instance, *Pseudomonas aeruginosa* secrets abundant exopolysaccharides to form a more robust biofilm than *E. coli*, demonstrating a remarkable self-healing activity after mechanical yielding [39–41]. In addition, the biofilm that forms in a confined environment becomes sturdier and denser than that forms on a flat substrate [42]. Therefore, it is essential to engineer a more powerful microrobot that can clean *P. aeruginosa* biofilm in confined space.

To this end, this study demonstrates a self-locomotive, antimicrobial microrobot (SLAM) swarm that can generate oxygen bubbles at controlled rates and eliminate biofilm via collective microbubbling (Scheme 1). The SLAMs are rod-shaped, hollow diatom particles loaded with manganese oxide (MnO_2) nanocatalysts, which endow the SLAMs with the ability to self-propel in hydrogen peroxide (H_2O_2) solution by ejecting oxygen (O_2) microbubbles from the diatom's hollow channel. We hypothesize that SLAMs doped with a critical mass of manganese oxide (MnO_2) nanocatalysts would self-assemble into a swarm due to the interaction between microbubbles from diatoms. The resulting SLAM swarm would surround a microbubble and repeat microbubble generation and burst to continuously provide cavitation energy sufficient to fracture biofilms and, in turn, decrease bacterial resistance to antibiotics and disinfectants.

To examine this hypothesis, first, we improved our previously

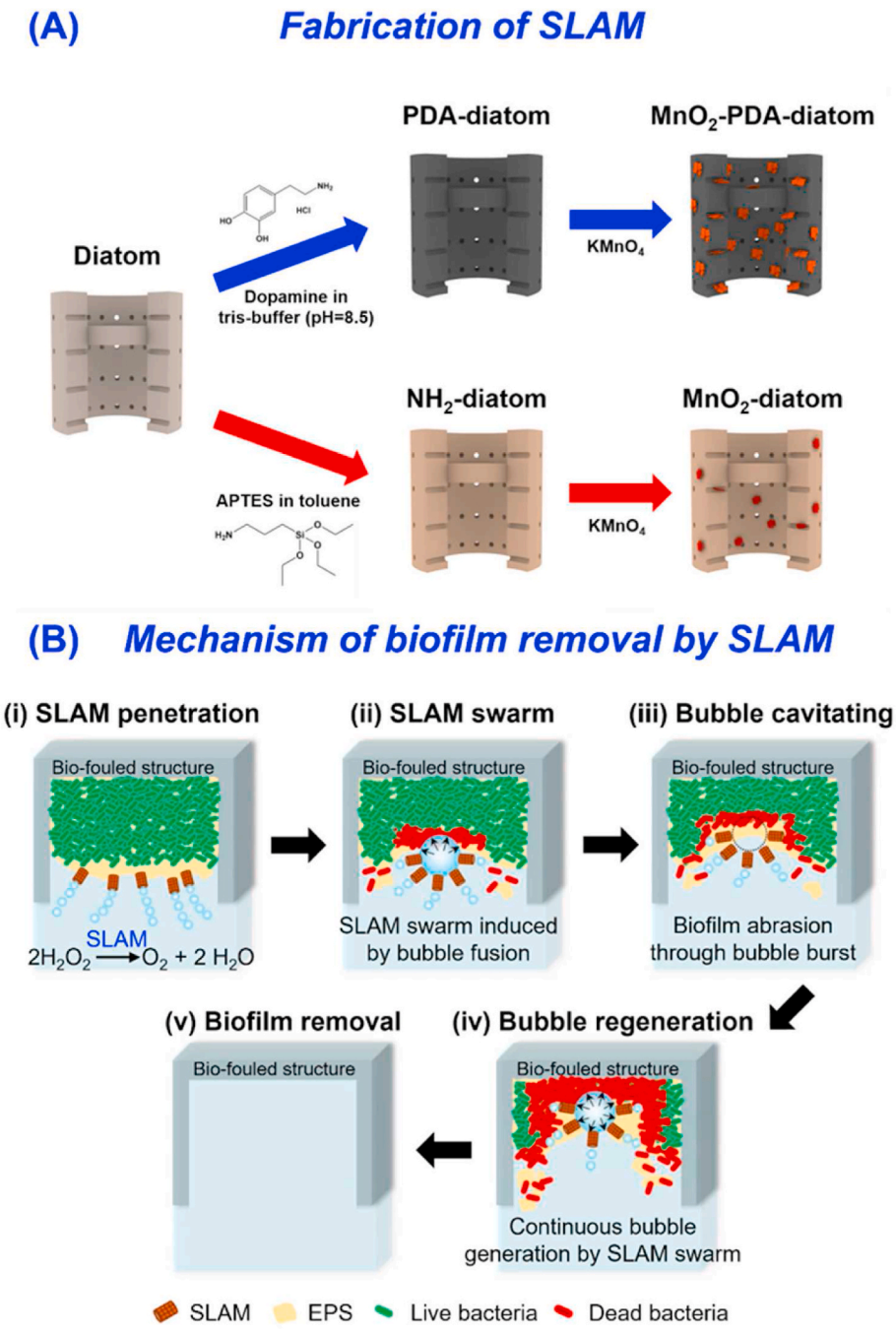

Scheme 1. Fabrication of SLAM and its mechanism for biofilm removal. (A) The SLAMs are assembled by doping MnO_2 on diatom particles through polydopamine (PDA) coating (top: MnO_2-PDA-diatom) and grafting of (3-aminopropyl)triethoxysilane (APTES) (bottom: MnO_2-diatom). (B) The mechanism of biofilm removal by SLAM: (i) The SLAMs firstly penetrate the biofilm through self-propulsion. (ii) The SLAMs further self-assemble into a swarm that keeps generating a microbubble to fracture the EPS of biofilm. (iii) The microbubble formed by SLAM swarm bursts to generate cavitation energy sufficient to abrade biofilms. (iv) The SLAM swarm repeats microbubble generation and burst to fracture biofilms continuously. (v) The SLAM swarm completely removes biofilms from the bio-fouled structure in the end.

developed diatom microbubbler by increasing the loading mass of MnO_2 nanocatalysts on diatoms using polydopamine (PDA) binder. Second, we examined the extent that the loading mass of MnO_2 on diatoms regulates the microbubble generation, self-propulsion speed, kinetic reaction, and swarm formation. Then, we analyzed the frequency of repeated bubble generation and burst in the swarm and proposed a mechanism that controls the swarming behavior of SLAMs. Finally, we evaluated the efficacy in cleaning *P. aeruginosa* biofilms covering microgrooved silicone structure and wounded porcine skin explants, along with irrigating water or antibiotics.

2. Materials and methods

2.1. Fabrication of MnO_2-PDA-diatom and MnO_2-diatom particles

The MnO_2-PDA-diatom particles were fabricated via PDA coating. First, to remove impurity and debrides, 200 mg of diatom particles (DiatomaceousEarth-food grade, amorphous silica from freshwater type) were washed with deionized water and collected by centrifugation for 3 min at 1000 rpm. The washing process was repeated three times. The resultant particle slurry was mixed with 320 mL of deionized water containing 100 mg of dopamine hydrochloride (Sigma-Aldrich) under the stirring condition at 500 rpm. After 1 h, 80 mL of Tris-HCl solution (50 mM, pH = 8.5) was added into the mixture and stirred for 24 h at room temperature to polymerize dopamine. The diatom particles were collected by centrifugation at 1000 rpm for 3 min and washed with deionized water three times. The particles, denoted as PDA-diatom, were dried overnight in a lyophilizer (Labconco). Second, 50 mg of PDA-diatom particles were mixed with 5 mL of 50 mM $KMnO_4$ (Sigma-Aldrich) solution and stirred at 500 rpm for 2 h. Then, the particles were collected by centrifugation at 1000 rpm for 3 min and washed with deionized water three times. The sample, denoted as MnO_2-PDA-diatom, was dried in a lyophilizer overnight.

Separately, the MnO_2-diatom particles were fabricated through grafting with (3-aminopropyl)triethoxysilane (APTES, Sigma-Aldrich). First, 2 g of purified diatom particles was mixed with 60 mL of toluene in a three-necked flask coupled with a reflux condenser under an N_2 atmosphere. Then, 0.6 mL of deionized water was added to the mixture and stirred at room temperature for 2 h. To initiate the silane grafting, 3.4 mL of APTES was added to the mixture and stirred at 60 °C. After 6 h, the mixture was cooled down and then washed with toluene, 2-propanol, and deionized water three times. The obtained particles, denoted as NH_2-diatom, were dried in a lyophilizer overnight. Second, 0.1 g of NH_2-diatoms were mixed with 1 mL of 50 mM $KMnO_4$ solution and sonicated for 30 min. Then, the particles were collected by centrifugation at 1000 rpm for 3 min and washed with deionized water three times. The sample, denoted as MnO_2-diatom, was dried in a lyophilizer overnight.

2.2. Characterizations of MnO_2-PDA-diatom and MnO_2-diatom particles

The morphology and elemental analysis of MnO_2-doped diatom particles were conducted using a scanning electron microscope (Hitachi S-4800 SEM) at 10 kV and 20 kV, respectively. The transmission electron microscopy (TEM) images were obtained by JEOL 2100 Cryo TEM with an accelerating voltage of 200 kV. The content of the manganese element was quantified by inductively coupled plasma mass spectrometry (ICP-MS, NexION 350D). The surface of MnO_2-doped particles was analyzed by X-ray photoelectron spectroscopy (XPS, Kratos Axis ULTRA). The motion of particles in the aqueous H_2O_2 solution was observed with an optical microscope (Leica DMIL). The speed and motion trajectory of particles were quantified and tracked by using Fiji software.

2.3. H_2O_2 decomposition kinetic analysis of MnO_2-doped diatom particles

The H_2O_2 decomposition reactivity was evaluated using batch reactors. Phosphate-buffered saline solutions were balanced with 30% H_2O_2 to give a desired H_2O_2 concentration (1 mM - 1 M) and agitated at 750 rpm. Most measurements were performed at ambient temperature, but the reactors were also placed in ice or oil baths to change the temperature for activation energy measurements, monitored with in situ thermocouples. A varying amount of catalytic material was added to the reactor to give a constant Mn concentration (1 mM) across all measurements. After the addition of the catalyst, aliquots were withdrawn every 1 min for 5 min and filtered. These aliquots were diluted in H_2O to H_2O_2 concentrations below 0.2 mM and titrated with equal volumes of an H_2O_2 indicator solution (75 v% H_2O, 25 v% CH_3CH_2OH, 4.1 mM $CuSO_4$, 6.0 mM neocuproine). These titrated samples were aged 30 min to allow for saturation and analyzed with a UV–Vis spectrometer (Spectronic, Genesys 20). To measure H_2O_2 concentrations, the absorbance at 454 nm for each sample was compared to a calibration curve [43] obtained using standard solutions of known concentration.

2.4. Analysis of the MnO_2-PDA-diatom swarm

The swarming clusters formed by MnO_2-PDA-diatoms in 1.5–10 wt% H_2O_2 solutions were recorded using an optical microscope (Axio Observer D1, Carl Zeiss, Inc.) coupled with a high-speed camera (Phantom Miro eX4) at 1000 fps. The time-lapse images were extracted by Fiji software. The volume of the individual O_2 bubble was calculated by measuring the diameter of the bubble. The transient volumetric change was further obtained by taking the time derivative at each time point.

2.5. Preparation of biofilm on microgrooved poly(dimethylsiloxane) (PDMS) substrate

First, the PDMS prepolymer and curing agent (SYLGARD 184 Silicone Elastomer Kit, Dow Corning) were mixed at a mass ratio of 10:1 for 3 min. The mixture was then degassed in a vacuum desiccator. After 10 min, the mixture was slowly poured onto a silicon master with a microgrooved pattern (100 μm in width) and cured at 60 °C overnight in the oven. The cured PDMS with a microgrooved pattern was gently peeled off from the silicon master and treated with plasma (Harrick plasma, plasma cleaner PDC-32G) to expose silanol groups on its surface. The microgrooved PDMS substrate was further sterilized with 70% ethanol as well as UV exposure for 30 min. Secondly, *P. aeruginosa* (ATCC 15442) was streaked for isolation on a Trypticase™ Soy Agar (TSA) plate (BD BBL™) and cultured at 37 °C overnight. Then, 3 to 5 isolated colonies were inoculated in 200 mL of Tryptic Soy Broth (TSB) broth (BD Bacto™) for 20 h at 37 °C on a shaker at 100 rpm. The concentration of *P. aeruginosa* was subsequently adjusted to an optical density (OD_{600}) of 0.2, which corresponded to CFU/mL of 10^8. The bacterial cell suspension (200 μL) was transferred onto the microgrooved PDMS substrate and incubated at 37 °C. After 24 h, the microgrooved PDMS substrate was gently rinsed with sterile phosphate-buffered saline (PBS, Corning) to remove planktonic bacterial cells. Then, fresh bacterial cell suspension (200 μL, OD_{600} = 0.2) was added onto the microgrooved PDMS substrate and incubated at 37 °C for another 24 h. This process was repeated until the third day of biofilm growth. After 3 days, the biofilms on the microgrooved PDMS substrate were rinsed with sterile PBS before further analysis.

2.6. Biofilm removal from the microgrooved PDMS substrate

The 3-day old *P. aeruginosa* biofilms on the microgrooved PDMS substrate were treated with 3 wt% H_2O_2 solution, MnO_2-diatom in 3 wt % H_2O_2 solution, and MnO_2-PDA-diatom in 3 wt% H_2O_2 solution. 500 μL of H_2O_2 solution with or without particles was added to a 6-well plate in

each treatment. Then, PDMS substrate was placed in each well for treatment. After 10 min, the treated PDMS substrates were gently rinsed with PBS to remove the H_2O_2 solution and diatom particle residues for further analysis.

2.7. Evaluation of biofilm removal efficacy with the microgrooved PDMS substrate

Crystal violet staining was performed to evaluate the efficacy of biofilm removal quantitively. After each treatment, the PDMS substrates with biofilms were immersed in the 0.1 wt% crystal violet (Sigma-Aldrich) solution for 30 min. The substrates were then rinsed with PBS to remove excess crystal violet, followed by immersion in 95% ethanol to dissolve crystal violet within the biofilm. The efficacy of biofilm removal for each treatment was determined by measuring the absorbance intensity of crystal violet at a wavelength of 550 nm on a microplate reader (TECAN, Switzerland).

2.8. Immunostaining of EPS in the biofilm

First, the protein in the biofilms was labeled by incubating the PDMS substrate with biofilms in 500 μL of 0.1 M $NaHCO_3$ buffer (pH = 9.2) containing 5 mg of fluorescein isothiocyanate (Sigma-Aldrich) for 1h [44]. Second, the substrate with biofilms was rinsed with PBS. The substrate was incubated with 500 μL of 250 μg mL^{-1} concanavalin A, tetramethylrhodamine conjugate (Invitrogen) for 2h to label α-glucopyranosyl and α-mannopyranosyl polysaccharide residues. Again, the substrate with biofilms was rinsed with PBS and incubated in 500 μL of 300 μg mL^{-1} brightener 28 (MP Biomedicals, LLC) to label β-linked polysaccharides. Finally, the substrate with biofilms was mounted on a glass-bottom dish for observation using a confocal laser scanning microscope (Zeiss LSM 700, Germany).

2.9. Preparation of porcine skin explants with a puncture wound

The preparation of porcine skin explants was modified from previous literature [45]. First, fresh porcine skin purchased from a local merchandiser was frozen at −80 °C freezer overnight. The frozen porcine skin was subsequently excised into explants with a diameter of 12 mm by using a biopsy punch. Then, a hand-held drill (Dremel® 7700–1) with a high-speed cutter (Dremel® 191) was used to consistently create a central wound site with 2 mm diameter and 1 mm depth on the explant. Second, the porcine skin explants were immersed in PBS containing 5 μL L^{-1} Tween-80 (Sigma-Aldrich) to remove any foreign debris. After 10 min, the explants were transferred to 70% ethanol (prepared with PBS solution containing 5 μL L^{-1} Tween-80) for another 30 min. Finally, the explants were washed with PBS containing 5 μL L^{-1} Tween-80 for 10 min, repeating 3 times. The whole sterilization process was conducted on a shaker.

2.10. Biofilm growth in a puncture wound of porcine skin explants

P. aeruginosa (ATCC 15442) was streaked for isolation on a Trypticase™ Soy Agar (TSA) plate (BD BBL™) and cultured at 37 °C overnight. Then, 3–5 isolated colonies were inoculated in 200 mL of Tryptic Soy Broth (TSB) (BD Bacto™) for 20 h on a shaker at 100 rpm. The concentration of *P. aeruginosa* was subsequently adjusted to an optical density (OD_{600}) of 0.2, which corresponded to CFU mL^{-1} of 10^8. Next, sterile porcine skin explants were placed on soft 0.5% agar TSA with 50 μg mL^{-1} gentamicin in a 24-well plate. Then, 5 μL of 10^8 CFU mL^{-1} *P. aeruginosa* was inoculated in the central wound site of each explant. The 24-well plate was covered with the lid and cultured in an incubator at 37 °C for 3 days.

2.11. Biofilm removal from a puncture wound of porcine skin explants

After 3-day culture, the bottom of a skin explant with biofilm was fixed on a sterile lid of a 24-well plate by super glue. At the same time, the rinse plates were prepared by adding 3 mL of PBS in each well of a sterile 24-well plate. The testing plate was prepared by adding 3 mL of PBS, 3 wt% H_2O_2 solution, or 3 wt% H_2O_2 solution with MnO_2-PDA-diatom particles. To begin the test, the lid with explants was quickly placed onto the first rinse plate for 10 s to remove planktonic bacterial cells. Then, the lid was transferred to a testing plate for the biofilm removal test. After 10 min of treatment, the lid was removed from the testing plate and put on the second rinse plate for another 10 s to remove any biofilm debris. The control group was treated only with the first rinse plate.

2.12. Evaluation of biofilm removal efficacy from a puncture wound of skin explants

The explants were transferred in a 15 mL centrifugation tube containing 7 mL of sterile PBS with 5 μL L^{-1} Tween-80. Catalase (Sigma-Aldrich) was added to obtain a concentration of 2 mg mL^{-1} solution to neutralize the H_2O_2 residue if necessary. Then, a sonication probe (Fisher Scientific Model 100) was applied in each tube at 20 W in an ice bath for 30 s to separate the bacteria into suspension. The probe was disinfected with 70% ethanol between sampling. The suspension was serially diluted by 10-fold, spot plated on TSA plates, and incubated at 37 °C overnight. Colonies in a countable range of 2–20 in each spot were recorded and converted as colony-forming units per milliliter (CFU mL^{-1}), standing for the viable bacterial concentration.

2.13. SEM imaging of the biofilm in a puncture wound of skin explants

First, the explants were fixed in 0.1 M Na-Cacodylate buffer (pH = 7.4) containing 2.0% paraformaldehyde and 2.5% glutaraldehyde (both E.M. grade) in the fridge. After 4 h, the explants were rinsed with 0.1 M Na-Cacodylate buffer for 10 min on a shaker and then dehydrated with a progressively higher concentration of ethanol, namely, 37% (10 min), 67% (10 min), 95% (10 min), and 100% (10 min for 3 times). Second, the fixative explants were dried using a critical point dryer in 100% ethanol. The morphology of explants was obtained by environmental SEM (FEI Quanta FEG 450 ESEM) at 2 kV.

2.14. Optical coherence tomography (OCT) imaging of a biofilm-infected wound

Each sample was non-destructively imaged by a custom-built spectral-domain optical coherence tomography (SD-OCT) system [46]. The OCT system utilized a superluminescent diode (S5FC1325S-SP, Thorlabs, New Jersey) with a center wavelength of 1325 nm and a bandwidth of 50 nm as a light source. A spectrometer with a 1024-pixel InGaAs line-scan camera (SU-LDH2, Goodrich, North Carolina) was used as a detector that acquired spectra at a line scan rate of approximately 92 kHz. The OCT system had an axial and transverse resolution of approximately 8 μm and 16 μm, respectively. Each cross-sectional OCT image represented 3.13 mm (depth) and 4.18 mm (width). The OCT images were acquired using LabVIEW and processed using MATLAB.

2.15. Post-treatments of biofilm

After treatments with MnO_2-PDA-diatoms or controls, the biofilm residues were further treated with either irrigation or antibiotics. For irrigation, the puncture wound site was rinsed with 5 mL of PBS using a 20 mL syringe coupled with an 18-gauge needle. The explants were immediately probe-sonicated to separate the biofilm debris and spot-plated to evaluate the biofilm removal efficacy. For antibiotics treatment, each porcine skin explant was immersed in 2 mL media containing

200 μg mL^{-1} gentamicin and incubated at 37 °C. After 24 h, the porcine skin explants were rinsed with PBS. The number of viable microbial cells was quantified with the spot-plating method mentioned above.

2.16. Statistical analysis

Three samples were analyzed per condition, and the data were presented as mean ± standard deviation unless otherwise specified. One-way ANOVA followed by Turkey's post hoc analyses was performed for comparisons between groups to determine significance. Data were considered statistically significant with p values less than 0.05.

3. Results and discussion

3.1. Synthesis and characterizations of MnO_2 sheet-doped diatoms

The SLAM was assembled by using binding agents to incorporate MnO_2 nanosheets on the surfaces of diatom biosilica particles (Scheme 1A). The hollow cylinder-shaped diatom particles with 10 μm-diameter, 18 μm-length, and 500 nm-diameter pores (Fig. 1A) were modified with the PDA binder. The PDA layer was formed through self-polymerization of dopamine activated by a weak alkaline tris buffer solution (pH = 8.5) [47,48]. The dopamine concentration was optimized at 0.25 mg mL^{-1} to form a uniform PDA layer on the diatom surface (Fig. 1B; Fig. S1). As shown in the transmission electron microscopy (TEM) image (Fig. 1C), the PDA layer thickness is around 50 nm compared to the TEM image of bare diatom surface (Fig. S2). Particle color was also changed from white to black because of the PDA layer (Fig. S3A, B).

The PDA-diatom particles were further loaded with MnO_2 sheets by reducing permanganate ions (MnO_4^-) as follows [49]:

$$MnO_4^- + 2H_2O + 3e^- \text{ (electron donors: PDA)} \rightarrow MnO_2 + 4OH^- \quad (1)$$

The PDA binder on diatoms served as an agent that enhances reduction of MnO_4^- into MnO_2 in situ and forms MnO_2 sheets on the diatom surface, as confirmed with the TEM image (Fig. 1D). The resulting MnO_2 changed the powder color from black to brown, indicating the MnO_2 sheets formation (Fig. S3C). The elemental mapping shows the uniform coverage of the PDA-diatoms with the MnO_2 sheets (Fig. 1E). The elemental analysis by inductively coupled plasma-atomic emission spectroscopy (ICP-AES) further shows that the loading amount of Mn element is 18.2 wt%.

As a point of comparison, MnO_2-diatoms were prepared by modifying diatom surface to present primary amine groups using (3-aminopropyl)triethoxysilane binder (Scheme 1A) [28]. Then, MnO_4^- was reduced to form the MnO_2 sheets on the diatom surface. The elemental mapping images confirmed Mn immobilized on the diatoms, but the Mn coverage was lower than MnO_2-PDA-diatoms (Fig. 1F). According to ICP-AES measurement, the loading amount of Mn element was 2.5 wt% on the MnO_2-diatoms, which was 7.3-fold lower than the MnO_2-PDA--diatom. This difference is because PDA offers abundant catechol groups to trigger the reduction of ionic MnO_4^- into solid MnO_2.

We also examined the chemical composition of the pristine diatom, PDA-diatom, and MnO_2-PDA-diatom surface using X-ray photoelectron spectroscopy (XPS) (Fig. 1G–J). The peaks of Si 2s (153.0 eV) and Si 2p (100.2 eV) from the pristine diatom were consistent with unmodified biosilica SiO_2 [50]. The intensity of these two peaks sharply decreased after modification, indicating the surface coverage by the PDA layer and MnO_2 sheets (Fig. 1G). We further confirmed the PDA layer on diatoms using the high-resolution N 1s XPS (Fig. 1H). The N 1s peak at 400.0 eV in PDA-diatom was fitted into three peaks at 398.6 eV, 399.9 eV, and 401.9 eV. Each of the peaks represented tertiary/aromatic (R–N = , 11.50%), secondary (R_2-N-H, 74.21%), and primary (R–NH_2, 14.29%) amine groups of PDA, respectively [51]. This N 1s signal disappeared after forming MnO_2 sheets on the PDA-diatom (Fig. S4). The two peaks in Mn 2p spectrum at 642.1 eV (Mn $2p_{3/2}$) and 653.8 eV (Mn $2p_{1/2}$) with spin-energy separation of 11.7 eV (Fig. 1I) and the two peaks in Mn 3s spectrum with the spin-energy separation of 4.7 eV (Fig. 1J) indicate the existence of Mn^{4+} on the PDA-diatoms [49,52,53].

3.2. Effects of MnO_2 mass on the self-propulsion speed of MnO_2-doped diatoms

We examined the extent that MnO_2 sheets regulate the propulsion speed of diatoms. First, MnO_2-PDA-diatoms and MnO_2-diatoms were fixed on a separate glass slide immersed in the 5 wt% H_2O_2 solution to measure the O_2 bubble generation rate. Initially, a tiny O_2 bubble embryo emerged from the hollow channel of both MnO_2-PDA-diatom and MnO_2-diatom (0 ms in Fig. 2A). The O_2 bubble embryo grew over 260 ms with the MnO_2-PDA-diatom and 410 ms with the MnO_2-diatom. The O_2 bubble growth rate of the MnO_2-PDA-diatom was 1.6-fold higher than the MnO_2-diatom. As the bubble diameter reached ~12 μm, the bubble was separated from the diatom. The bubble generation and ejection continued until the H_2O_2 was consumed. As a control, the unmodified diatoms did not generate a bubble (Fig. S5).

The movement of diatoms is consistent with the vast majority of O_2 bubbles forming within the hollow diatoms rather than on the diatom exterior. Previous studies [54,55] indicate that bubble nucleation energy barriers are much lower on concave than on convex surfaces, considering the cylindrical diatom morphology, agrees with the previous observation. Though MnO_2 may be distributed throughout the diatom interior and exterior, the O_2 bubble preferentially form in the interior concave channels (Fig. 2B). The 7-fold larger loading of MnO_2 within MnO_2-PDA-diatoms than upon MnO_2-diatoms leads to a proportional increase in the rate of O_2 generation, bubble growth, and ejection frequency.

The bubbles ejected from the diatom's hollow channel generate thrust to make the particles self-propel in the H_2O_2 solution. As shown in Fig. 2C, both MnO_2-PDA-diatoms and MnO_2-diatoms self-propelled by O_2 bubbles released continuously from the channel of diatom (Movie S1-S4). The propulsion speed of the MnO_2-PDA-diatom was highly dependent on the H_2O_2 concentration, increasing from 106 ± 16 μm s^{-1} in 2 wt% H_2O_2 solution to 270 ± 41 μm s^{-1} in 10 wt% H_2O_2 solution (Fig. 2D). In contrast, the propulsion speed of MnO_2-diatom was less dependent on the H_2O_2 concentration, ranging from 27 ± 8 μm s^{-1} in 2 wt% H_2O_2 solution to 98 ± 29 μm s^{-1} in 10 wt% H_2O_2 solution.

Supplementary video related to this article can be found at https://doi.org/10.1016/j.biomaterials.2022.121610

The difference in the self-propulsion speed between MnO_2-PDA-diatom and MnO_2-diatom was related to the decomposition rate of H_2O_2 to O_2. As shown in Fig. 2E, the initial H_2O_2 decomposition rate was linearly dependent on the H_2O_2 concentration for the MnO_2-PDA-diatoms (rate ~ $[H_2O_2]^{0.9\pm0.1}$). In contrast, MnO_2-diatoms led to a sub-linear dependency of initial H_2O_2 decomposition rate on the H_2O_2 concentration (rate ~ $[H_2O_2]^{0.7\pm0.1}$). These observations are consistent with the kinetics of H_2O_2 dependence on transition metal-modified silicates and suggest a bimolecular reaction between fluid-phase H_2O_2 and H_2O_2-derived Mn-complex [56–58]. On average, the H_2O_2 decomposition rate based on per gram of the MnO_2-PDA-diatoms was 11-fold higher than the MnO_2-diatoms.

We also calculated the apparent activation energy (E_a) for H_2O_2 decomposition by fitting curves of the H_2O_2 decomposition rate versus temperature to the Arrhenius Equation (Fig. S6). The E_a obtained with MnO_2-PDA-diatom was 26 ± 3 kJ mol^{-1}, while that with MnO_2-diatoms was 29 ± 3 kJ mol^{-1}. This similar E_a, together with a nearly first-order dependence upon H_2O_2 concentration suggests that both MnO_2-PDA-diatoms and MnO_2-diatoms decompose H_2O_2 by similar mechanisms. Overall, the number of H_2O_2 decomposition sites changes from MnO_2-PDA-diatom to MnO_2-diatom but not the inherent reactivity of those sites.

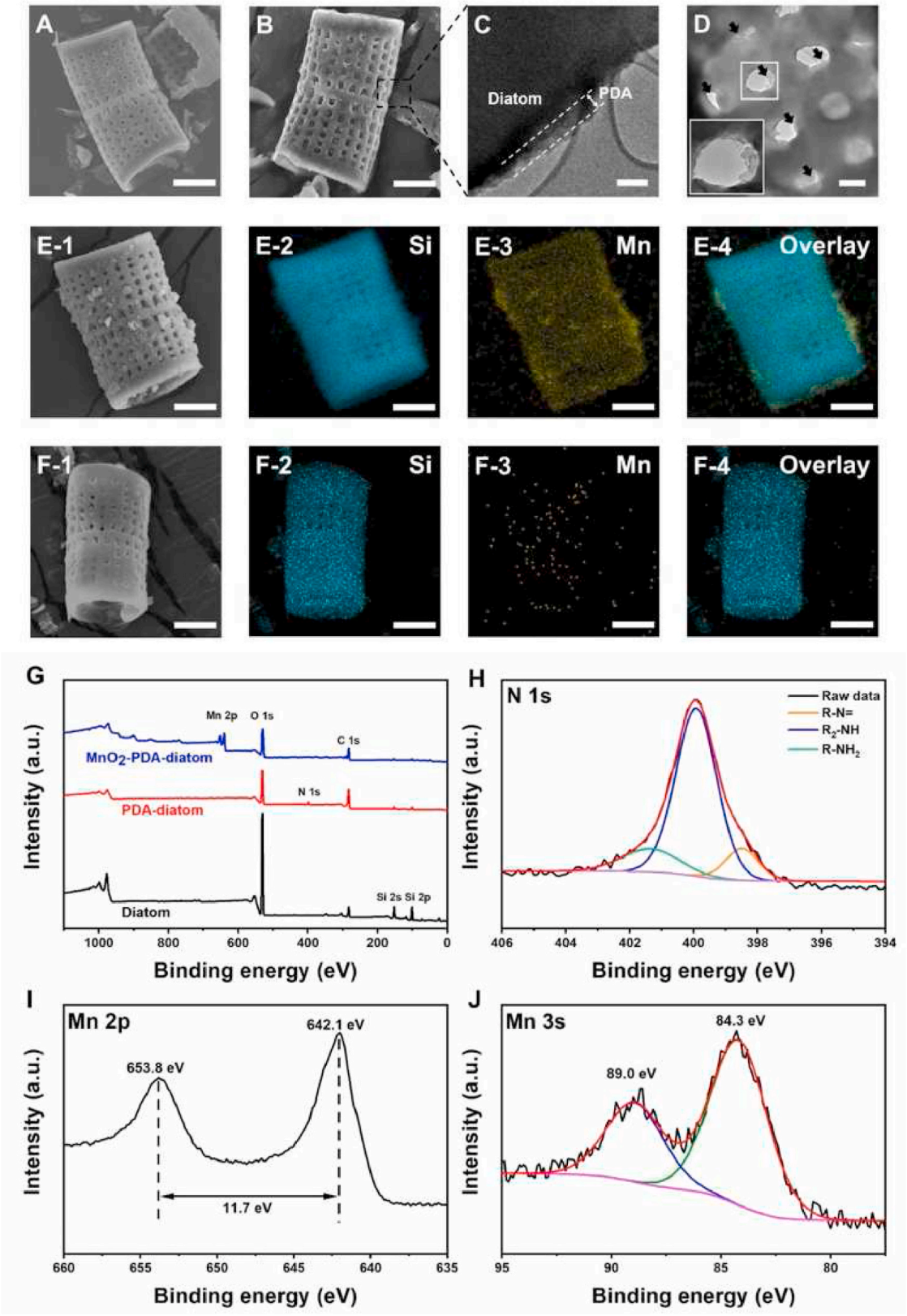

Fig. 1. Characterizations of MnO_2-PDA-diatom. (A) SEM image of a pristine diatom. Scale bar: 5 μm. (B) SEM image of PDA-diatom. Scale bar: 5 μm. (C) TEM image of PDA-diatom. Scale bar: 100 nm. (D) TEM images of MnO_2-PDA-diatom. Arrows indicate the MnO_2 deposited on the PDA layer. Inset image of (D) represents the higher magnification of MnO_2-PDA assembled around the side pore wall. Scale bar: 100 nm. (E, F) SEM and elemental mapping images of (E) MnO_2-PDA-diatom and (F) MnO_2-diatom. Scale bar: 5 μm. (G–J) XPS spectra of pristine diatoms, PDA-diatom, and MnO_2-PDA-diatom particles. (G) XPS survey spectrum of pristine diatom, PDA-diatom, and MnO_2-PDA-diatom particles. (H) Deconvolution of high-resolution XPS spectrum of PDA-diatom for N 1s. (I, J) High-resolution XPS spectrum of MnO_2-PDA-diatom particles for (I) Mn 2p and (J) Mn 3s.

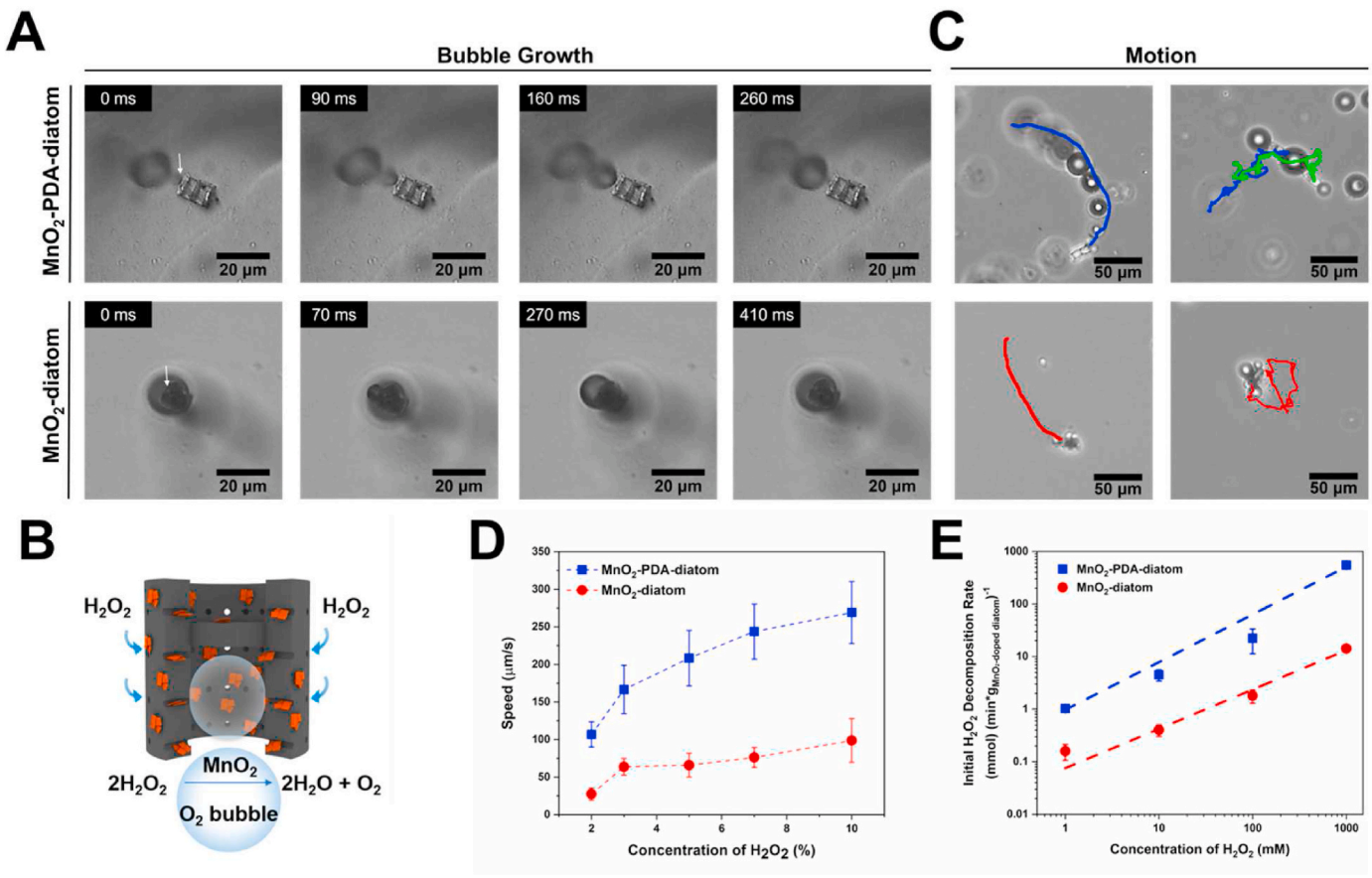

Fig. 2. Motion and kinetic analysis of MnO_2-PDA-diatom and MnO_2-diatom in H_2O_2 solutions. (A) Time-lapse images of microbubble generation from a fixed MnO_2-PDA-diatom and MnO_2-diatom in 5 wt% H_2O_2 solution. (B) Schematic illustration for the mechanism of bubble generation from a hollow channel of the MnO_2-doped diatom. (C) Time-lapse images of trajectories of the MnO_2-PDA-diatom and the MnO_2-diatom in 5 wt% H_2O_2 solution. (D) Self-propulsion speed of MnO_2-PDA-diatom and MnO_2-diatom particles in H_2O_2 solutions with varied H_2O_2 concentrations. (E) The dependency of the initial H_2O_2 decomposition rate on the H_2O_2 concentration for MnO_2-PDA-diatom and MnO_2-diatom. Data points represent the mean, and error bars indicate standard deviation. (n = 10 in (D) and n = 3 in (E)).

3.3. *Self-assembly of MnO_2-PDA-diatom swarm*

Next, we examined the interaction between SLAMs and their capability of forming a swarm through the microbubble interaction. To evaluate whether the concentration of SLAMs would play a role on the swarm formation, the concentration of SLAMs in 5 wt% H_2O_2 was increased from 0.032 mg mL^{-1} to 1 mg mL^{-1}. As shown in Fig. S7, MnO_2-PDA-diatoms self-propelled individually at low particle concentrations. However, they started self-assembling to form swarms at 0.25 mg mL^{-1} and higher concentrations. In particular, diatoms interacted more frequently at the higher particle concentration. As shown in Movie S5, the MnO_2-PDA-diatoms swarm created an O_2 bubble with 100 μm in diameter at the center. The O_2 bubble burst rapidly to let the swarm continue to create a new O_2 bubble. This repeated bubble generation and burst made the diatoms keep the swarm pattern without falling apart. Likewise, MnO_2-diatoms also formed swarms at 0.25 mg mL^{-1} and higher particle concentration (Fig. S7). However, the O_2 bubble at the center of the swarm expanded more slowly and aggregated with neighboring bubbles instead of burst (Movie S6).

Supplementary data related to this article can be found at https://doi.org/10.1016/j.biomaterials.2022.121610.

To study the reason causing this difference, we firstly investigated the interaction between MnO_2-PDA-diatoms and the subsequent O_2 bubble generation at 0.25 mg mL^{-1} with various concentrations of H_2O_2 using a high-speed camera (Fig. 3A; Movie S7). As shown in Fig. 3A–i and Movie S7, MnO_2-PDA-diatoms added to 10 wt% H_2O_2 solution instantaneously initiated self-propulsion. At the same time, 20 μm diameter O_2 bubbles hanging on the MnO_2-PDA-diatoms collided with each other and fused to form a single bubble within 30 ms. As a consequence, MnO_2- PDA-diatoms formed a swarm that surrounded the bubble. The bubble continued to grow with additional O_2 produced from the swarmed diatoms over the next 28 ms. The bubble finally burst at 59 ms. Even after the bubble burst, the diatoms kept the swarmed form, likely due to a local pressure depression. Then, the diatoms repeated the fresh O_2 bubble growth and burst (Movie S7). Such rapid oscillatory bubble formation and rupture caused by the MnO_2-PDA-diatom swarm was observed when H_2O_2 concentration was higher than 2 wt% (Fig. 3A–i to Fig. 3A–v). However, decreasing the H_2O_2 concentration from 10 to 2 wt% decreased the frequency of O_2 bubble growth and burst in a swarm from 16.9 to 4.2 bubbles per second. When the H_2O_2 concentration was decreased to 1.5 wt%, MnO_2-PDA-diatoms generated O_2 bubbles very slowly. Accordingly, the O_2 bubbles fused slowly into a larger bubble without bursting over 4688 ms, which acts like quasi-static bubble growth (Movie S7).

Supplementary data related to this article can be found at https://doi.org/10.1016/j.biomaterials.2022.121610.

We further quantified the O_2 bubble volume (V_b) increased over time before burst (Fig. 3B). In the beginning, there was a minimal increase of V_b regardless of H_2O_2 concentration because O_2 bubbles were at the stage of collision. Then, V_b increased sharply over time as diatoms formed a swarm around the O_2 bubble and supplied O_2 gas in a collective manner. Given that O_2 mass generated by MnO_2-PDA-diatoms determines V_b, we calculated the transient O_2 generation rate with time derivative (dV_b/dt) as shown in Fig. 3B. In 2 to 10 wt% H_2O_2 solutions,

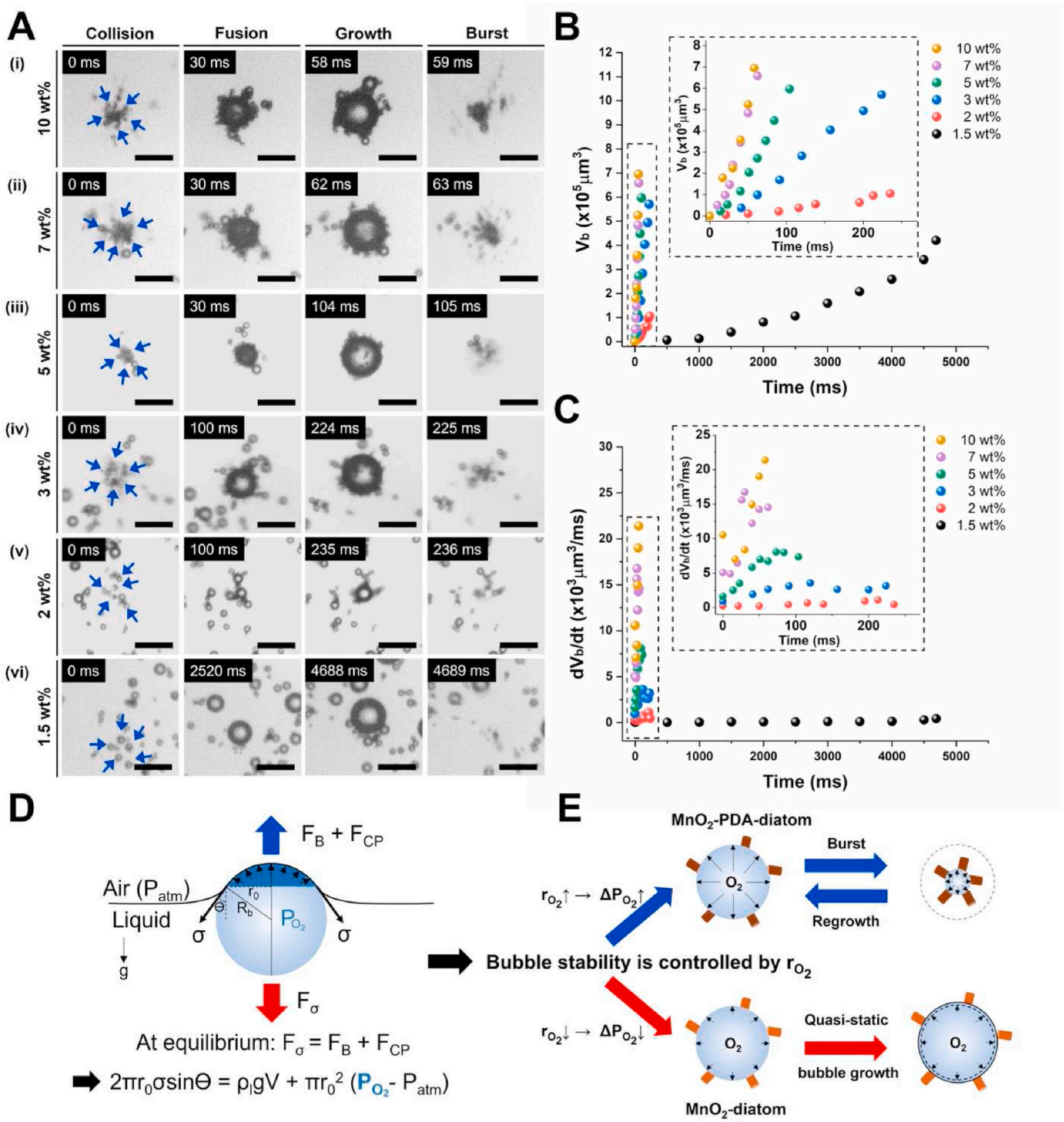

Fig. 3. Analysis of swarming by MnO_2-PDA-diatoms. (A) Time-lapse images of a cycle of O_2 bubble growth and rupture manipulated by the MnO_2-PDA-diatoms in aqueous media with varied H_2O_2 concentrations: (A-i) 10 wt%, (A-ii) 7 wt%, (A-iii) 5 wt%, (A-iv) 3 wt%, (A-v) 2 wt%, (A-vi) 1.5 wt%. The images were captured using a high-speed camera (1000 fps). The blue arrows in images captured at 0 ms indicate individual MnO_2-PDA-diatom that moves and forms a swarm. Scale bar: 100 μm. (B) The volume of O_2 bubble (V_b) increased over time in H_2O_2 solutions. The inset plot represents the curves in the dash line box. The V_b was calculated by assuming a spherical shape ($V_b = 4/3\pi r_b^3$). (C) The transient change of V_b with time (dV_b/dt) in H_2O_2 solutions. The inset plot represents the curves in the dash line box. (D) Schematic illustration of force balance on a growing O_2 bubble at the air-liquid interface. (E) Schematic illustration of bubble fates altered by the O_2 generation rate of MnO_2-PDA-diatoms and MnO_2-diatoms. (For interpretation of the references to color in this figure legend, the reader is referred to the Web version of this article.)

dV_b/dt increased over time, indicating the accelerated bubble growth (Fig. 3C). The acceleration of dV_b/dt became larger with increasing H_2O_2 concentration, while dV_b/dt remained constant over time in 1.5 wt% H_2O_2 solution. Moreover, the dV_b/dt at the time when the bubble burst was almost linearly dependent on the H_2O_2 concentration from 2 to 10 wt% (Fig. S8).

Based on the results above, we suggest that the accelerated bubble growth over time leads to the bubble burst. In general, as shown in

Fig. 3D, there are three forces acting on a growing bubble at the air/water interface: buoyancy force F_B, capillary force F_σ, and contact pressure force F_{CP} [59,60]. Before the bubble ruptures, the sum of these forces should remain zero (Fig. 4D):

$$\vec{F_B} + \vec{F_\sigma} + \vec{F_{CP}} = 0 \quad (2)$$

Equation (2) can be further expanded by the definition of each term:

$$2\pi r_0 \sigma \sin\theta = \rho_l g V + \pi r_0^2 (P_{O_2} - P_{atm}) \quad (3)$$

where r_0 is the radius of bubble cross-section at the air-liquid interface, σ is the surface tension, θ is the instantaneous contact angle, ρ_l is the density of the liquid, g is the acceleration due to gravity, V is the bubble volume below the air-liquid interface, P_{O2} is the O_2 bubble pressure, and P_{atm} is the atmospheric pressure. According to Equation (3), the surface tension holds the dynamic stability of a bubble while P_{O2} steadily keeps increasing due to the increase of the number of O_2 molecules.

The accelerated rise of P_{O2} may disrupt the dynamic stability and, finally, cause the bubble to burst. The P_{O2} inside the bubble is estimated by applying kinetic measurement of MnO_2-PDA-diatom particles as follows (see Supplementary data for a detailed derivation):

$$P_{O_2} - P_{atm} = 0.2425 C_{diatom} C_{0,\ H_2O_2} RTt \quad (4)$$

where C_{diatom} is the concentration of MnO_2-PDA-diatom particles and $C_{0,\ H2O2}$ is the initial concentration of H_2O_2. As shown in Fig. S9, the pressure difference between bubble and atmosphere increases faster at higher H_2O_2 concentrations. However, the pressure difference between bubble and atmosphere at the moment of bubble burst converges at 350–550 Pa, independent of H_2O_2 concentrations. Therefore, O_2 bubbles burst more frequently in the higher H_2O_2 concentration. After the first O_2 bubble burst, MnO_2-PDA-diatom swarms continue to decompose H_2O_2 to O_2, thus repeating the bubble growth and burst with the same frequency. The significantly reduced O_2 bubble growth and burst frequency in the 1.5 wt% H_2O_2 solution is attributed to the delayed P_{O2} increase and constant dV_b/dt. Separately, MnO_2-diatoms added into the H_2O_2 solution exhibited quasi-static bubble growth (Fig. S10) due to the 11-fold lower O_2 generation rate than the MnO_2-PDA-diatoms. The O_2 bubbles generated from MnO_2-diatoms either burst with a significantly lower frequency than MnO_2-PDA-diatoms or remained stable without burst (Fig. S10 and Fig. 3E). The quasi-static bubble growth with MnO_2-diatoms was observed at any H_2O_2 concentrations (Fig. S11).

3.4. Activities of MnO_2-doped diatoms to remove biofilm in confined space

Pseudomonas aeruginosa, as one of the prevalent pathogens, has been shown to have the ability to form robust biofilms due to its secretion of abundant exopolysaccharides [39–41]. According to our measurement, *P. aeruginosa* biofilm has a storage modulus more than two times greater than that of *E. coli* biofilm (Fig. S12). Therefore, we examined whether the swarming behavior of SLAMs could further bring a synergistic efficacy on the removal of a tougher *P. aeruginosa* biofilm in a microgrooved polydimethylsiloxane (PDMS) substrate (Fig. 4A). As shown in Fig. 4B–ii, biofilm exposed to the 3 wt% H_2O_2 solution generated O_2

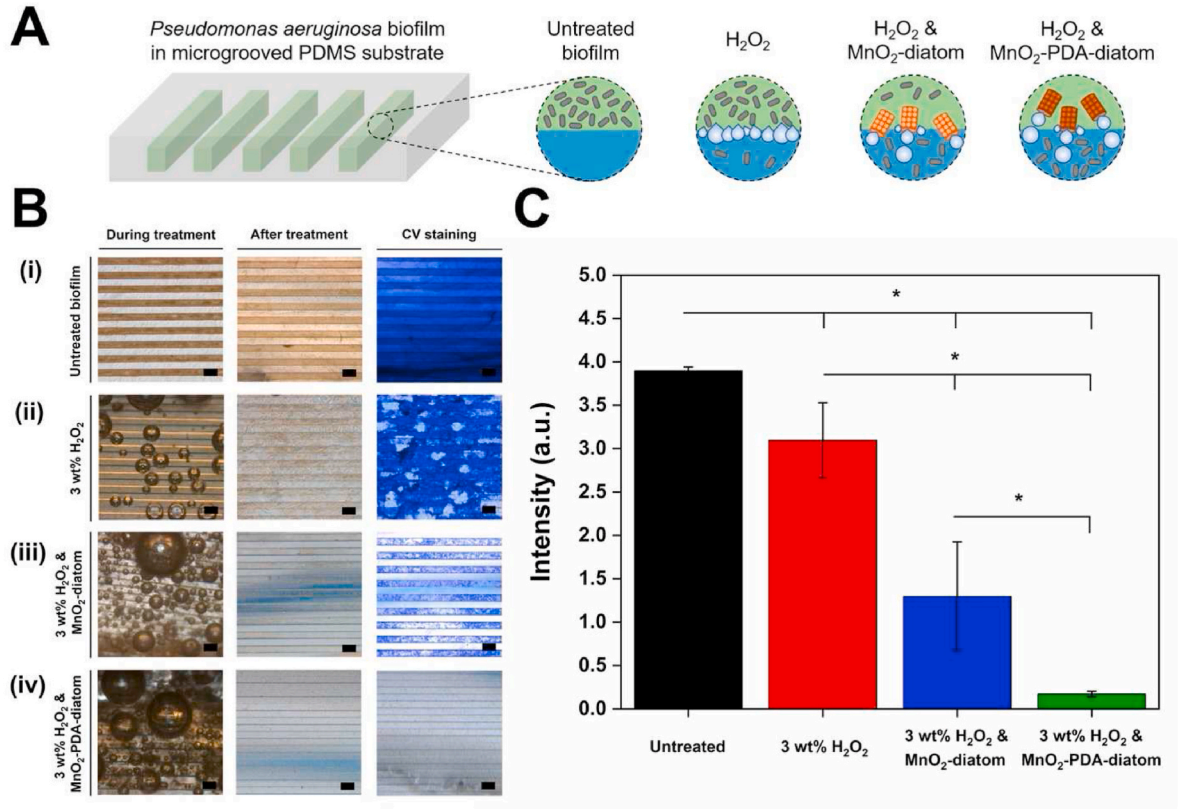

Fig. 4. Evaluation of *P. aeruginosa* biofilm removal from a microgrooved PDMS substrate. (A) Schematic illustration of conditions used to remove biofilm: untreated, 3 wt% H_2O_2 solution, 3 wt% H_2O_2 solution with MnO_2-diatom, and 3 wt% H_2O_2 solution with MnO_2-PDA-diatom. (B) Optical images of PDMS substrate with biofilms for each treatment: (i) untreated biofilms, (ii) 3 wt% H_2O_2 solution, (iii) 3 wt% H_2O_2 solution with MnO_2-diatom, and (iv) 3 wt% H_2O_2 solution with MnO_2-PDA-diatom. The images in the first column represent the treatment at an intermediate stage (*i.e.*, 2 min after treatment starts). The images in the second column represent the PDMS substrate with biofilm after treatment for 10 min. The images in the third column represent the biofilm stained with crystal violet (CV) after treatment for 10 min. Scale bar: 200 μm. (C) Intensity of biomass remained on the PDMS substrate after each treatment for 10 min. Bars represent the average value, and error bars indicate standard deviation. * represents significant difference between the two groups, *$p < 0.05$ ($n = 5$). (For interpretation of the references to color in this figure legend, the reader is referred to the Web version of this article.)

bubbles on the surface because endogenous catalase within the biofilm decomposed H_2O_2 (Movie S8) [61]. However, most of the biofilm remained in the grooved substrate after exposure for 10 min. The biofilm residue was also stained with crystal violet [62], which binds with EPS and bacterial cells. Only about 20.5% of biofilm was removed from the PDMS substrate (Fig. 4C). In contrast, both MnO_2-diatoms and MnO_2-PDA-diatoms suspended in the 3 wt% H_2O_2 solution entered biofilm and generated microbubbles (Fig. 4B–iii, 4B-iv; Movie S9, S10). After 10 min, MnO_2-diatoms and MnO_2-PDA-diatoms removed ~66.7% and ~95.6% of biofilms, respectively (Fig. 4C). The biofilm removal efficacy was also confirmed by analyzing the residual EPS with immunostaining [44]. As shown in Fig. S13, most EPS consisting of α-glucopyranosyl/α-mannopyranosyl sugar residues (red), β-linked polysaccharides (blue), and extracellular proteins (green) remained in microgrooves after the treatment with the 3 wt% H_2O_2 solution. The mixture of H_2O_2 and MnO_2-diatoms removed a significant fraction of EPS. More strikingly, the mixture of H_2O_2 and MnO_2-PDA-diatom removed the EPS almost perfectly, as evidenced with minimal fluorescence signal.

Supplementary data related to this article can be found at https://doi.org/10.1016/j.biomaterials.2022.121610.

To understand the mechanism by which MnO_2-PDA-diatoms removed the biofilm more effectively than MnO_2-diatoms, we examined self-propulsion and O_2 generation of diatoms within the 3D biofilm microscopically. As shown in Fig. 5A and Movie S11, MnO_2-diatoms mixed with 3 wt% H_2O_2 solution penetrated the biofilm first. The O_2 bubbles generated by MnO_2-diatoms collided (0 s) and fused into a larger bubble (1.94 s). Then, the O_2 bubbles continued to expand and displaced the biofilm gradually (4.62 s). The O_2 bubbles remained stable for more than 10 s without further deforming or detaching the biofilm (Movie S11). In contrast, a larger number of MnO_2-PDA-diatoms penetrated biofilm than MnO_2-diatoms because of the higher self-propulsion speed. They continued to generate O_2 bubbles within the biofilm (Fig. 5B). Those O_2 bubbles collided (0 s) and fused to form larger bubbles surrounded by the diatom swarm (1.93 s). The resulting swarm drove O_2 bubbles to expand more rapidly than MnO_2-diatoms (4.53 s). The O_2 bubbles finally burst to create a cavity that drove dislocation and detachment of biofilm from the microgrooves (5.38 s). After the burst, the MnO_2-PDA-diatoms kept the swarmed form and repeated a cycle of bubble generation, fusion, and rupture (Movie S12).

Supplementary data related to this article can be found at https://doi.org/10.1016/j.biomaterials.2022.121610.

We suggest the more frequently repeated growth and burst of O_2 bubbles by MnO_2-PDA-diatoms exert powerful mechanical perturbation within the 3D biofilm by deforming and cavitating EPS of the biofilm. On the other hand, MnO_2-diatoms damage biofilm less effectively than MnO_2-PDA-diatoms as the O_2 bubbles from MnO_2-diatoms expand more slowly while causing minimal cavitation energy.

3.5. *The ability of MnO_2-PDA-diatoms to treat biofilm-infected wounds in skin explants*

Topical treatment with 3% H_2O_2 solution has been extensively used for wound cleaning [63]. However, recent clinical studies suggest that H_2O_2 may not effectively reduce the bacterial burdens in wounds [63,64]. To this end, we further evaluated whether incorporating MnO_2-PDA-diatoms into H_2O_2 could provide synergistic effects to clean biofilm-infected wounds. Before the test, we firstly evaluated the skin response to topical treatment with 3 wt% H_2O_2 and MnO_2-PDA--diatoms/3 wt% H_2O_2. The *in vivo* results indicate that neither 3 wt% H_2O_2 solution nor MnO_2-PDA-diatoms/3 wt% H_2O_2 mixture caused any irritation issue on the back skin (Fig. S14). In addition, the histology

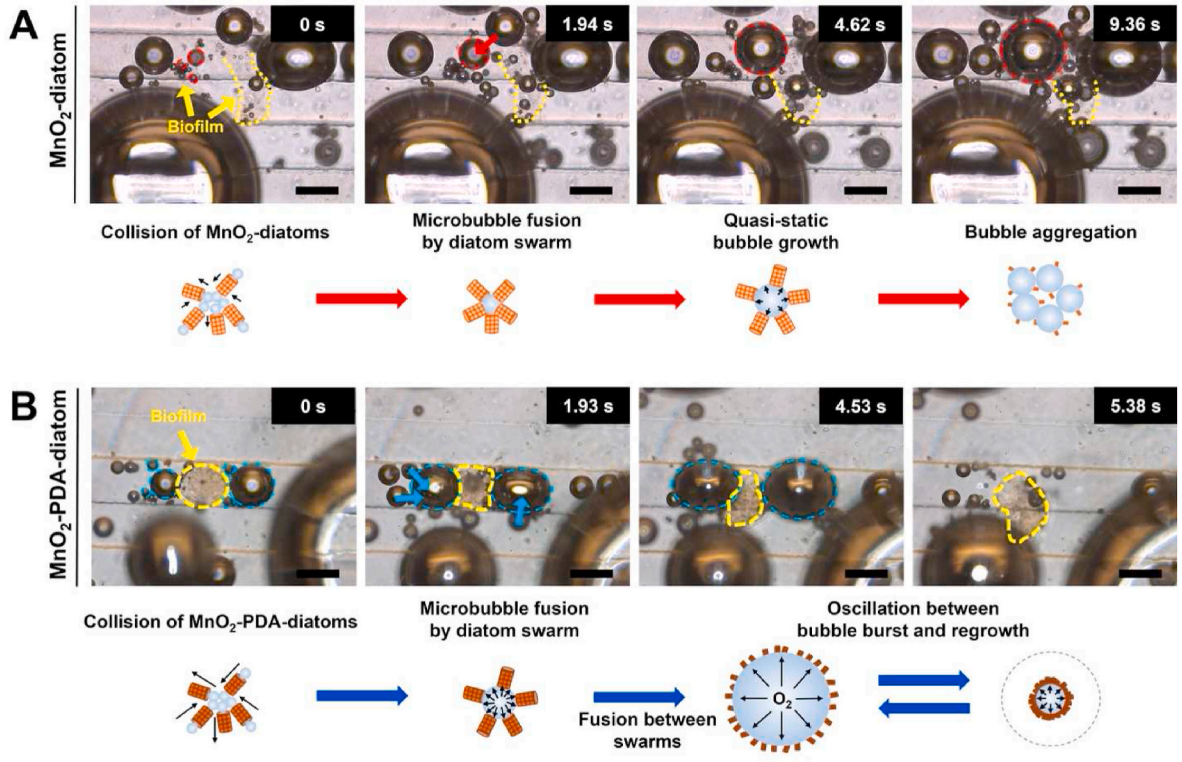

Fig. 5. Time-lapse images of *P. aeruginosa* biofilm removal process by O_2 bubbles from MnO_2-doped diatoms with a corresponding schematic illustration. (A) Treatment with MnO_2-diatoms mixed with 3 wt% H_2O_2 solution. The yellow arrows and dash line indicate the location of biofilm. The red-dash circles represent the O_2 bubbles generated by MnO_2-diatoms. (B) Treatment with MnO_2-PDA-diatoms mixed with 3 wt% H_2O_2 solution. The yellow arrow and dash line indicate the biofilm in the microgroove. The blue-dash circles represent the O_2 bubbles generated by the MnO_2-PDA-diatom swarm. Scale: 100 μm. (For interpretation of the references to color in this figure legend, the reader is referred to the Web version of this article.)

analysis also suggests both treatments did not result in any damage on the epidermal and dermal tissues on the skin (Fig. S15). Then, we created the biofilm in a punctured porcine skin explant by inoculating the wound site with *P. aeruginosa* for 3 days (Fig. 6A) [45,65], followed by the treatments with 3 wt% H_2O_2 and MnO_2-PDA-diatoms/3 wt% H_2O_2 mixture (Fig. S16). Optical coherence tomography (OCT) was used to evaluate the biofilm removal efficacy (Fig. 6B), allowing for non-invasive and label-free 3D tissue imaging [66–69]. The OCT image of a biofilm-free punctured skin wound shows a hollow hole with a diameter of 2 mm and a depth of 1 mm (Fig. 6B–i). Three days after the punctured wound site was inoculated with *P. aeruginosa*, the wound site had become filled with the growth of a 0.5 mm-thick biofilm (Fig. 6B–ii). Adding 3 wt% H_2O_2 solution to the biofilm-infected wounds generated O_2 bubbles by endogenous catalase. This treatment damaged the superficial layer of biofilm only (Fig. 6B–iii). In contrast, the MnO_2-PDA-diatoms/3 wt% H_2O_2 mixture created many deeper and larger craters, marked with negative contrast, in the biofilm (Fig. 6B–iv).

In parallel, we imaged the biofilm that remained in the wounds using scanning electron microscopy (SEM) (Fig. 6C). Fig. 6C–i displays collagen fibers at the bottom part of the punctured, biofilm-free wound in the porcine skin. After 3-day culture of *P. aeruginosa*, the collagen fibers of skin tissue were covered with a thick layer of biofilms and planktonic bacterial cells (Fig. 6C–ii), as also shown in the OCT image. The wound treated with 3 wt% H_2O_2 solution was covered with rod-shaped bacterial cells associated with EPS (Fig. 6C–iii). In contrast, biofilm-infected wounds treated with MnO_2-PDA-diatoms/3 wt% H_2O_2 mixture for 10 min revealed collagen fibers that resemble the pristine skin wound, indicating that the treatment could remove biofilm with minimal perturbation on the surrounding tissues (Fig. 6C–iv). We suggest that this successful biofilm removal results from penetration of MnO_2-PDA-diatoms into the biofilm as shown in Fig. 6D and subsequent O_2 bubble growth and rupture by diatom swarms within the biofilm. We also quantified the number of viable cells that remained in wounds using the spot plate count method [70,71]. The treatment with 3 wt% H_2O_2 solution reduced viable *P. aeruginosa* cells by 72.2% (Fig. 6E). In contrast, the MnO_2-PDA-diatoms/3 wt% H_2O_2 mixture decreased the number of viable cells more significantly by 99.2%.

We further examined whether the biofilm treated with MnO_2-PDA-diatoms/3 wt% H_2O_2 mixture became more susceptible to the conventional processes used to remove the biofilm in the wound. These processes include water irrigation and treatment with the antibiotic gentamicin. Irrigating the biofilm-infected wound reduced viable *P. aeruginosa* cells by 81.4% (Fig. 6E). Infected wound treated with 3 wt % H_2O_2 solution for 10 min and subsequent irrigation made additional 40% reduction, resulting in an 83.3% total reduction (Fig. 6E). These results combined with OCT and SEM images (Fig. 6B–iii, 6C-iii) indicated both irrigation only and irrigation following 3 wt% H_2O_2 solution removed the planktonic cells on the superficial layer of biofilm. The EPS

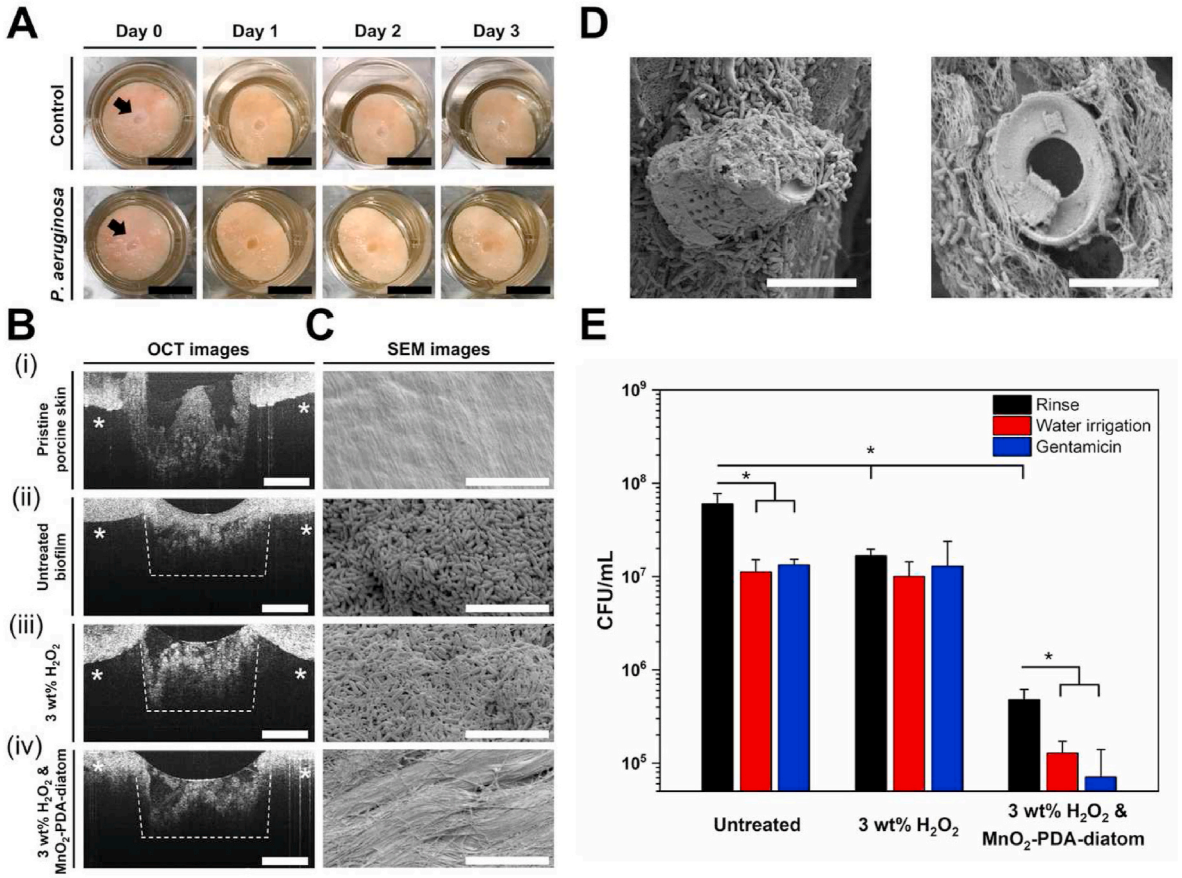

Fig. 6. Removal of *P. aeruginosa* biofilm infecting the puncture wounds created in the porcine skin explant. (A) Image of 2 mm-diameter puncture wound in porcine skin explants. The arrows indicate the location of the puncture wound site on the porcine skin explant. Scale bar: 1 cm. (B, C) Optical coherence tomography (OCT) and scanning electron microscope (SEM) images of infected wound sites in porcine skin explants: (i) pristine porcine skin without biofilm, (ii) porcine skin infected by biofilm, (iii) biofilm-infected wound after treatment with 3 wt% H_2O_2 solution for 10 min, and (iv) biofilm-infected wound after treatment with MnO_2-PDA-diatom and 3 wt% H_2O_2 solution for 10 min. The asterisks in (B) indicate an area with mirror artifacts due to the limited imaging depth in SD-OCT. Scale bar: 1 mm in (B) and 10 μm in (C). (D) SEM images of MnO_2-PDA-diatom particles that penetrate biofilm. Scale bar: 10 μm. (E) Microbial cell viability level after the treatments and post-treatment with water irrigation and gentamicin. The number of viable cells was quantified by colony-forming unit (CFU) plate counting. Bars represent the average value, and error bars indicate standard deviation. * represents significant difference between the two groups, *$p < 0.05$ ($n = 3$).

residues held bacterial cells together, thus becoming a mechanical barrier against irrigating water. In contrast, irrigation following the treatment with MnO_2-PDA-diatoms/3 wt% H_2O_2 mixture made an additional 73.3% reduction of viable cells, leading to a 99.8% total reduction. This result confirms that biofilm damaged by MnO_2-PDA-diatoms becomes vulnerable to the external force exerted by irrigation (Fig. 6E).

Separately, biofilm in wounds was treated with the antibiotic gentamicin. Wounds treated with gentamicin reduced viable bacterial cells by 77.8% (Fig. 6E). In addition, gentamicin administered after treatment with 3 wt% H_2O_2 solution made 22.9% additional reduction, resulting in a 78.6% total reduction. Similar to irrigation, either gentamicin only or gentamicin following 3 wt% H_2O_2 solution did not remove EPS, hence limiting the transport of both gentamicin and H_2O_2 through the biofilm. However, gentamicin administered after treatment with MnO_2-PDA-diatoms/3 wt% H_2O_2 mixture resulted in additional 85.1% reduction of viable cells, leading to 99.9% total reduction. This result also indicates that MnO_2-PDA-diatoms made biofilm residues permeable to gentamicin, thus increasing the antibiotic efficacy of gentamicin.

4. Conclusion

This study presents an active antimicrobial particle (SLAM) that can remove biofilm in abiotic and biotic structures (microgrooved substrates and puncture wounds) and subsequently decrease the number of viable bacterial cells. The SLAM was assembled by doping controlled amounts of MnO_2 nanosheets to porous diatoms using different binders. In particular, increasing Mn mass percentage in the diatom to 18.2 wt% using the polydopamine binder made the resulting MnO_2-PDA-diatoms penetrate the *P. aeruginosa* biofilm by generating O_2 bubbles in H_2O_2 solutions and forming a swarm. The resulting diatom swarms were active to repeat O_2 bubble generation and rupture, which created a wave of cavitating energy sufficient to fracture EPS and remove biofilm from the original fouled site. Furthermore, MnO_2-PDA-diatoms removed almost 99.9% of viable cells when combined with irrigation or antibiotics. In contrast, decreasing MnO_2 mass percentage in diatoms to 2.5 wt % through the APTES grafting method reduced biofilm removal efficacy because the slower O_2 bubble growth lowered the frequency of bubble generation and rupture to further remove biofilm residues. Such powerful cleaning activities would be further tuned with other catalysts, H_2O_2 concentrations, and temperature, thus enabling the SLAM broadly applicable to clean various biofilm-fouled tissue and infrastructure.

Credit author statement

Y.-H.D. and H.K. conceived and designed the experiments. T.R. and D.W.F. performed the H_2O_2 decomposition experiment and analysis. J. W. and S.A.B. performed the measurement for biofilm imaging with optical coherence tomography. M.A.W. and S.A.R. performed and analyzed the rheological property of biofilm. Y.-H.D. wrote the manuscript with input from all authors and performed the rest of the experiments.

Data availability

The data that support the findings of this study are available from the corresponding author upon reasonable request.

Declaration of competing interest

The authors declare that they have no known competing financial interests or personal relationships that could have appeared to influence the work reported in this paper.

Acknowledgements

We appreciate the National Science Foundation (NSF-DMR 2004719) and the SerVaas Lab. OCT imaging and processing was supported in part by grants from the National Institutes of Health (R01EB013723, R01EB028615, S.A.B.). Electron microscopy and XPS analysis were performed at the Frederick Seitz Materials Research Laboratory Central Facilities at the University of Illinois. ICP-AES was conducted at Microanalysis Laboratory (SCS CORES) at the University of Illinois. Electron microscopy and high-speed camera were performed at Beckman Institute Imaging Technology Group at the University of Illinois. Y.-H.D. and H.K. thank Dr. J.B.Stiethl (Stiehl Tech LLC) for the scientific discussion.

Appendix A. Supplementary data

Supplementary data to this article can be found online at https://doi.org/10.1016/j.biomaterials.2022.121610.

References

[1] Antimicrobial Resistance: Global Report on Surveillance, World Health Organization, 2014. https://apps.who.int/iris/handle/10665/112642.
[2] L. Hall-Stoodley, P. Stoodley, J.W. Costerton, P. Stoodley, D. Lebeaux, A. Chauhan, O. Rendueles, C. Beloin, L. Hall-Stoodley, J.W. Costerton, P. Stoodley, A. Stacy, L. McNally, S.E. Darch, S.P. Brown, M. Whiteley, Bacterial biofilms: from the natural environment to infectious diseases, Nat. Rev. Microbiol. 2 (2004) 95–108, https://doi.org/10.1038/nrmicro821.
[3] A. Stacy, L. McNally, S.E. Darch, S.P. Brown, M. Whiteley, The biogeography of polymicrobial infection, Nat. Rev. Microbiol. 14 (2016) 93–105, https://doi.org/10.1038/nrmicro.2015.8.
[4] L. Hall-Stoodley, P. Stoodley, Evolving concepts in biofilm infections, Cell Microbiol. 11 (2009) 1034–1043, https://doi.org/10.1111/j.1462-5822.2009.01323.
[5] D. Lebeaux, A. Chauhan, O. Rendueles, C. Beloin, From in vitro to in vivo models of bacterial biofilm-related infections, Pathogens 2 (2013) 288–356, https://doi.org/10.3390/pathogens2020288.
[6] N. Kip, J.A. van Veen, The dual role of microbes in corrosion, ISME J. 9 (2015) 542–551, https://doi.org/10.1038/ismej.2014.169.
[7] H.A. Videla, L.K. Herrera, Understanding microbial inhibition of corrosion. A comprehensive overview, Int. Biodeterior. Biodegrad. 63 (2009) 896–900, https://doi.org/10.1016/j.ibiod.2009.02.002.
[8] C.D. Rummel, A. Jahnke, E. Gorokhova, D. Kühnel, M. Schmitt-Jansen, Impacts of biofilm formation on the fate and potential effects of microplastic in the aquatic environment, Environ. Sci. Technol. Lett. 4 (2017) 258–267, https://doi.org/10.1021/acs.estlett.7b00164.
[9] M.P. Schultz, J.A. Bendick, E.R. Holm, W.M. Hertel, Economic impact of biofouling on a naval surface ship, Biofouling 27 (2011) 87–98, https://doi.org/10.1080/08927014.2010.542809.
[10] D. Davies, Understanding biofilm resistance to antibacterial agents, Nat. Rev. Drug Discov. 2 (2003) 114–122, https://doi.org/10.1038/nrd1008.
[11] H.C. Flemming, J. Wingender, U. Szewzyk, P. Steinberg, S.A. Rice, S. Kjelleberg, Biofilms: an emergent form of bacterial life, Nat. Rev. Microbiol. 14 (2016) 563–575, https://doi.org/10.1038/nrmicro.2016.94.
[12] H.C. Flemming, J. Wingender, The biofilm matrix, Nat. Rev. Microbiol. 8 (2010) 623–633, https://doi.org/10.1038/nrmicro2415.
[13] L. Kim, Riddle of biofilm resistance, Antimicrob. Agents Chemother. 45 (2001) 999–1007, https://doi.org/10.1128/AAC.45.4.999-1007.2001.
[14] K.K. Jefferson, What drives bacteria to produce a biofilm? FEMS (Fed. Eur. Microbiol. Soc.) Microbiol. Lett. 236 (2004) 163–173, https://doi.org/10.1016/j.femsle.2004.06.005.
[15] P.S. Stewart, Diffusion in biofilms, J. Bacteriol. 185 (2003) 1485–1491, https://doi.org/10.1128/JB.185.5.1485-1491.2003.
[16] D. Sharma, L. Misba, A.U. Khan, Antibiotics versus biofilm: an emerging battleground in microbial communities, Antimicrob. Resist. Infect. Control 8 (2019) 76, https://doi.org/10.1186/s13756-019-0533-3.
[17] H. Koo, R.N. Allan, R.P. Howlin, P. Stoodley, L. Hall-Stoodley, Targeting microbial biofilms: current and prospective therapeutic strategies, Nat. Rev. Microbiol. 15 (2017) 740–755, https://doi.org/10.1038/nrmicro.2017.99.
[18] C.A. Schütz, L. Juillerat-Jeanneret, H. Mueller, I. Lynch, M. Riediker, Therapeutic nanoparticles in clinics and under clinical evaluation, Nanomedicine 8 (2013) 449–467, https://doi.org/10.2217/nnm.13.8.
[19] M. Natan, E. Banin, From Nano to Micro: using nanotechnology to combat microorganisms and their multidrug resistance, FEMS (Fed. Eur. Microbiol. Soc.) Microbiol. Rev. 41 (2017) 302–322, https://doi.org/10.1093/femsre/fux003.
[20] Z. Rukavina, Ž. Vanić, Current trends in development of liposomes for targeting bacterial biofilms, Pharmaceutics 8 (2016), https://doi.org/10.3390/pharmaceutics8020018.

[21] K. Forier, K. Raemdonck, S.C. de Smedt, J. Demeester, T. Coenye, K. Braeckmans, Lipid and polymer nanoparticles for drug delivery to bacterial biofilms, J. Contr. Release 190 (2014) 607–623, https://doi.org/10.1016/j.jconrel.2014.03.055.

[22] C. Li, E.J. Cornel, J. Du, Advances and prospects of polymeric particles for the treatment of bacterial biofilms, ACS Appl. Polym. Mater. 3 (2021) 2218–2232, https://doi.org/10.1021/acsapm.1c00003.

[23] T.-F.C. Mah, G.A. O'Toole, Mechanisms of biofilm resistance to antimicrobial agents, Trends Microbiol. 9 (2001) 34–39, https://doi.org/10.1016/S0966-842X(00)01913-2.

[24] S. Fulaz, S. Vitale, L. Quinn, E. Casey, Nanoparticle–biofilm interactions: the role of the EPS matrix, Trends Microbiol. 27 (2019) 915–926, https://doi.org/10.1016/j.tim.2019.07.004.

[25] D.S.W. Benoit, H. Koo, Targeted, triggered drug delivery to tumor and biofilm microenvironments, Nanomedicine 11 (2016) 873–879, https://doi.org/10.2217/nnm-2016-0014.

[26] Y. Liu, H.J. Busscher, B. Zhao, Y. Li, Z. Zhang, H.C. van der Mei, Y. Ren, L. Shi, Surface-adaptive, antimicrobially loaded, micellar nanocarriers with enhanced penetration and killing efficiency in staphylococcal biofilms, ACS Nano 10 (2016) 4779–4789, https://doi.org/10.1021/acsnano.6b01370.

[27] B. Horev, M.I. Klein, G. Hwang, Y. Li, D. Kim, H. Koo, D.S.W. Benoit, pH-activated nanoparticles for controlled topical delivery of farnesol to disrupt oral biofilm virulence, ACS Nano 9 (2015) 2390–2404, https://doi.org/10.1021/nn507170s.

[28] Y. Seo, J. Leong, J.D. Park, Y.T. Hong, S.H. Chu, C. Park, D.H. Kim, Y.H. Deng, V. Dushnov, J. Soh, S. Rogers, Y.Y. Yang, H. Kong, Diatom microbubbler for active biofilm removal in confined spaces, ACS Appl. Mater. Interfaces 10 (2018) 35685–35692, https://doi.org/10.1021/acsami.8b08643.

[29] K. Villa, J. Viktorova, J. Plutnar, T. Ruml, L. Hoang, M. Pumera, Chemical microrobots as self-propelled microbrushes against dental biofilm, Cell Rep. Phys. Sci. 1 (2020), 100181, https://doi.org/10.1016/j.xcrp.2020.100181.

[30] T. Cui, S. Wu, Y. Sun, J. Ren, X. Qu, Self-propelled active photothermal nanoswimmer for deep-layered elimination of biofilm in vivo, Nano Lett. 20 (2020) 7350–7358, https://doi.org/10.1021/acs.nanolett.0c02767.

[31] D. Vilela, N. Blanco-Cabra, A. Eguskiza, A.C. Hortelao, E. Torrents, S. Sanchez, Drug-free enzyme-based bactericidal nanomotors against pathogenic bacteria, ACS Appl. Mater. Interfaces 13 (2021), https://doi.org/10.1021/acsami.1c00986, 14964–14973.

[32] M. Ussia, M. Urso, K. Dolezelikova, H. Michalkova, V. Adam, M. Pumera, Active light-powered antibiofilm ZnO micromotors with chemically programmable properties, Adv. Funct. Mater. 31 (2021), https://doi.org/10.1002/adfm.202101178, 2101178.

[33] Z. Lin, C. Gao, D. Wang, Q. He, Bubble-propelled janus gallium/zinc micromotors for the active treatment of bacterial infections, Angew. Chem. Int. Ed. 60 (2021) 8750–8754, https://doi.org/10.1002/anie.202016260.

[34] K. Yuan, B. Jurado-Sánchez, A. Escarpa, Dual-propelled lanbiotic based janus micromotors for selective inactivation of bacterial biofilms, Angew. Chem. Int. Ed. 60 (2021) 4915–4924, https://doi.org/10.1002/anie.202011617.

[35] K. Villa, H. Sopha, J. Zelenka, M. Motola, L. Dekanovsky, D.C. Beketova, J. M. Macak, T. Ruml, M. Pumera, Enzyme-photocatalyst tandem microrobot powered by urea for Escherichia coli biofilm eradication, Small n/a (2022), 2106612, https://doi.org/10.1002/smll.202106612.

[36] Y. Dong, L. Wang, K. Yuan, F. Ji, J. Gao, Z. Zhang, X. Du, Y. Tian, Q. Wang, L. Zhang, Magnetic microswarm composed of porous nanocatalysts for targeted elimination of biofilm occlusion, ACS Nano 15 (2021) 5056–5067, https://doi.org/10.1021/acsnano.0c10010.

[37] H. Geelsu, P.A. J, H.E. E, L. Yuan, B. Alaa, K. Bekir, S. Kathleen, K. Vijay, S. Edward, K. Hyun, Catalytic antimicrobial robots for biofilm eradication, Sci. Robot. 4 (2019), eaaw2388, https://doi.org/10.1126/scirobotics.aaw2388.

[38] H. Boudarel, J.-D. Mathias, B. Blaysat, M. Grédiac, Towards standardized mechanical characterization of microbial biofilms: analysis and critical review, Biofilm. Microbiom. 4 (2018) 17, https://doi.org/10.1038/s41522-018-0062-5.

[39] O. Lieleg, M. Caldara, R. Baumgärtel, K. Ribbeck, Mechanical robustness of Pseudomonasaeruginosa biofilms, Soft Matter 7 (2011) 3307–3314, https://doi.org/10.1039/C0SM01467B.

[40] M.T.T. Thi, D. Wibowo, B.H.A. Rehm, Pseudomonas aeruginosa biofilms, Int. J. Mol. Sci. 21 (2020), https://doi.org/10.3390/ijms21228671.

[41] C. Ryder, M. Byrd, D.J. Wozniak, Role of polysaccharides in Pseudomonas aeruginosa biofilm development, Curr. Opin. Microbiol. 10 (2007) 644–648, https://doi.org/10.1016/j.mib.2007.09.010.

[42] E.K. Chu, O. Kilic, H. Cho, A. Groisman, A. Levchenko, Self-induced mechanical stress can trigger biofilm formation in uropathogenic Escherichia coli, Nat. Commun. 9 (2018) 4087, https://doi.org/10.1038/s41467-018-06552-z.

[43] T. Ricciardulli, S. Gorthy, J.S. Adams, C. Thompson, A.M. Karim, M. Neurock, D. W. Flaherty, Effect of Pd coordination and isolation on the catalytic reduction of O2 to H2O2 over PdAu bimetallic nanoparticles, J. Am. Chem. Soc. 143 (2021) 5445–5464, https://doi.org/10.1021/jacs.1c00539.

[44] C. González-Machado, R. Capita, F. Riesco-Peláez, C. Alonso-Calleja, Visualization and quantification of the cellular and extracellular components of Salmonella Agona biofilms at different stages of development, PLoS One 13 (2018), e0200011.

[45] Q. Yang, P.L. Phillips, E.M. Sampson, A. Progulske-Fox, S. Jin, P. Antonelli, G. S. Schultz, Development of a novel ex vivo porcine skin explant model for the assessment of mature bacterial biofilms, Wound Repair Regen. 21 (2013) 704–714, https://doi.org/10.1111/wrr.12074.

[46] P.-C. Huang, E.J. Chaney, R.R. Iyer, D.R. Spillman, B. Odintsov, N.A. Sobh, S. A. Boppart, Interstitial magnetic thermotherapy dosimetry based on shear wave magnetomotive optical coherence elastography, Biomed. Opt Express 10 (2019) 539–551, https://doi.org/10.1364/BOE.10.000539.

[47] H. Lee, S.M. Dellatore, W.M. Miller, P.B. Messersmith, Mussel-inspired surface chemistry for multifunctional coatings, Science 318 (1979) 426–430, https://doi.org/10.1126/science.1147241, 2007.

[48] Y. Liu, K. Ai, L. Lu, Polydopamine and its derivative materials: synthesis and promising applications in energy, environmental, and biomedical fields, Chem. Rev. 114 (2014) 5057–5115, https://doi.org/10.1021/cr400407a.

[49] Y. Li, R. Zhao, S. Chao, B. Sun, C. Wang, X. Li, Polydopamine coating assisted synthesis of MnO2 loaded inorganic/organic composite electrospun fiber adsorbent for efficient removal of Pb2+ from water, Chem. Eng. J. 344 (2018) 277–289, https://doi.org/10.1016/j.cej.2018.03.044.

[50] P.J. Walsh, S.A. Clarke, M. Julius, P.B. Messersmith, Exploratory testing of diatom silica to map the role of material attributes on cell fate, Sci. Rep. 7 (2017), 14138, https://doi.org/10.1038/s41598-017-13285-4.

[51] R.A. Zangmeister, T.A. Morris, M.J. Tarlov, Characterization of polydopamine thin films deposited at short times by autoxidation of dopamine, Langmuir 29 (2013) 8619–8628, https://doi.org/10.1021/la400587j.

[52] D. Hou, H. Tao, X. Zhu, M. Li, Polydopamine and MnO2 core-shell composites for high-performance supercapacitors, Appl. Surf. Sci. 419 (2017) 580–585, https://doi.org/10.1016/j.apsusc.2017.05.080.

[53] H. Li, L. Jiang, Q. Cheng, Y. He, V. Pavlinek, P. Saha, C. Li, MnO2 nanoflakes/hierarchical porous carbon nanocomposites for high-performance supercapacitor electrodes, Electrochim. Acta 164 (2015) 252–259, https://doi.org/10.1016/j.electacta.2015.02.218.

[54] W. Huang, M. Manjare, Y. Zhao, Catalytic nanoshell micromotors, J. Phys. Chem. C 117 (2013) 21590–21596, https://doi.org/10.1021/jp4080288.

[55] N.H. Fletcher, Size effect in heterogeneous nucleation, J. Chem. Phys. 29 (1958) 572–576, https://doi.org/10.1063/1.1744540.

[56] D.T. Bregante, D.W. Flaherty, Periodic trends in olefin epoxidation over group IV and V framework-substituted zeolite catalysts: a kinetic and spectroscopic study, J. Am. Chem. Soc. 139 (2017) 6888–6898, https://doi.org/10.1021/jacs.7b01422.

[57] D.T. Bregante, N.E. Thornburg, J.M. Notestein, D.W. Flaherty, Consequences of confinement for alkene epoxidation with hydrogen peroxide on highly dispersed group 4 and 5 metal oxide catalysts, ACS Catal. 8 (2018) 2995–3010, https://doi.org/10.1021/acscatal.7b03986.

[58] E.Z. Ayla, D.S. Potts, D.T. Bregante, D.W. Flaherty, Alkene epoxidations with H2O2 over groups 4–6 metal-substituted BEA zeolites: reactive intermediates, reaction pathways, and linear free-energy relationships, ACS Catal. 11 (2021) 139–154, https://doi.org/10.1021/acscatal.0c03394.

[59] S. di Bari, D. Lakehal, A.J. Robinson, A numerical study of quasi-static gas injected bubble growth: some aspects of gravity, Int. J. Heat Mass Tran. 64 (2013) 468–482, https://doi.org/10.1016/j.ijheatmasstransfer.2013.04.002.

[60] A. Georgoulas, P. Koukouvinis, M. Gavaises, M. Marengo, Numerical investigation of quasi-static bubble growth and detachment from submerged orifices in isothermal liquid pools: the effect of varying fluid properties and gravity levels, Int. J. Multiphas. Flow 74 (2015) 59–78, https://doi.org/10.1016/j.ijmultiphaseflow.2015.04.008.

[61] J.G. Elkins, D.J. Hassett, P.S. Stewart, H.P. Schweizer, T.R. McDermott, Protective role of catalase in Pseudomonas aeruginosa biofilm resistance to hydrogen peroxide, Appl. Environ. Microbiol. 65 (1999) 4594–4600, https://doi.org/10.1128/AEM.65.10.4594-4600.1999.

[62] F. Harold, Crystal violet binding capacity and the Gram reaction of bacterial cells, J. Bacteriol. 67 (1954) 689–691, https://doi.org/10.1128/jb.67.6.689-691.1954.

[63] E.C. Murphy, A.J. Friedman, Hydrogen peroxide and cutaneous biology: translational applications, benefits, and risks, J. Am. Acad. Dermatol. 81 (2019) 1379–1386, https://doi.org/10.1016/j.jaad.2019.05.030.

[64] G. Zhu, Q. Wang, S. Lu, Y. Niu, Hydrogen peroxide: a potential wound therapeutic target, Med. Princ. Pract. 26 (2017) 301–308, https://doi.org/10.1159/000475501.

[65] Q. Yang, C. Larose, A.C. della Porta, G.S. Schultz, D.J. Gibson, A surfactant-based wound dressing can reduce bacterial biofilms in a porcine skin explant model, Int. Wound J. 14 (2017) 408–413, https://doi.org/10.1111/iwj.12619.

[66] G.J. Tearney, M.E. Brezinski, B.E. Bouma, S.A. Boppart, C. Pitris, J.F. Southern, J. G. Fujimoto, In vivo endoscopic optical biopsy with optical coherence tomography, Science (1979) 276, https://doi.org/10.1126/science.276.5321.2037, 1997, 2037–2039.

[67] J.G. Fujimoto, M.E. Brezinski, G.J. Tearney, S.A. Boppart, B. Bouma, M.R. Hee, J. F. Southern, E.A. Swanson, Optical biopsy and imaging using optical coherence tomography, Nat. Med. 1 (1995) 970–972, https://doi.org/10.1038/nm0995-970.

[68] C. Xi, D.L. Marks, S. Schlachter, W. Luo, S.A.B. MD, High-resolution three-dimensional imaging of biofilm development using optical coherence tomography, J. Biomed. Opt. 11 (2006) 1–6, https://doi.org/10.1117/1.2209962.

[69] C.T. Nguyen, W. Jung, J. Kim, E.J. Chaney, M. Novak, C.N. Stewart, S.A. Boppart, Noninvasive in vivo optical detection of biofilm in the human middle ear, Proc. Natl. Acad. Sci. Unit. States Am. 109 (2012) 9529–9534, https://doi.org/10.1073/pnas.1201592109.

[70] S. Sieuwerts, F.A.M. de Bok, E. Mols, W.M. de Vos, J.E.T. van Hylckama Vlieg, A simple and fast method for determining colony forming units, Lett. Appl. Microbiol. 47 (2008) 275–278, https://doi.org/10.1111/j.1472-765X.2008.02417.

[71] P. Thomas, A.C. Sekhar, R. Upreti, M.M. Mujawar, S.S. Pasha, Optimization of single plate-serial dilution spotting (SP-SDS) with sample anchoring as an assured method for bacterial and yeast cfu enumeration and single colony isolation from diverse samples, Biotechnol. Rep. 8 (2015) 45–55, https://doi.org/10.1016/j.btre.2015.08.003.